THE JOURNAL OF PHYSICAL CHEMISTRY C
A JOURNAL OF THE AMERICAN CHEMICAL SOCIETY

pubs.acs.org/JPCC Article

Self-Organization and Nitrogen Incorporation in Diamond-Like Carbon Microstructures Synthesized by Nonthermal Plasma

Russell J. Clarke and Jason C. Hicks*

Cite This: *J. Phys. Chem. C* 2023, 127, 15239−15245

Read Online

ACCESS | Metrics & More | Article Recommendations | Supporting Information

ABSTRACT: Nonthermal plasma activation of light alkanes is an encouraging decarbonization strategy to produce chemicals or fuels from abundant and/or flared carbon sources. However, prolific carbon growth on both the catalyst and electrode has limited its practicality, requiring additional knowledge of the carbon structure and growth mechanism before breakthroughs are realized. Here, visual evidence is provided for nonuniform diamond-like carbon (DLC) microstructures that materialize in a coaxial dielectric barrier discharge (DBD) reactor flowing ethane and He at 278 K. Through a connection to known behaviors of DBD microdischarge patterns, the microstructure spacing was controlled by altering the applied voltage (ΔV) of the plasma or the burning voltage (U_b). Additionally, carbon valorization through nitrogen incorporation from N_2 was explored as an orthogonal solution to carbon mitigation, with N/C values >0.25 achieved and both sp^2 and sp^3 C−N bonding observed in the microstructures.

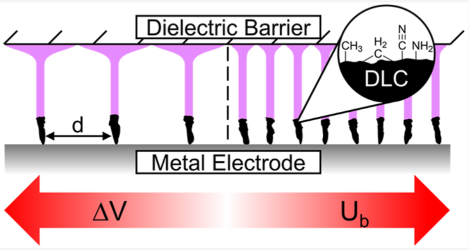

1. INTRODUCTION

The development of carbon-neutral technologies for point-source conversion of gaseous alkanes (e.g., biogas and shale gas) to energy-dense products and green hydrogen has received considerable attention in recent years.[1−6] Nonthermal plasma stimulation has emerged as a promising solution owing to its ease of coupling with renewable sources of electrical energy combined with its unique ability to reform natural gas at ambient conditions through inelastic collisions with high-energy electrons.[7] In a typical setup, an annular dielectric barrier discharge (DBD) plasma is combined with an appropriate catalyst in either a one- or two-stage process, resulting in enhancements to both the overall activity and product selectivity.[7−10] However, plasma-driven C−H and C−C bond scission in light alkanes leads to the uncontrolled formation of coke, which negatively affects the performance of both the catalyst and the plasma and presents a major barrier to commercial implementation.[11,12] Thus, achieving an advanced understanding of carbon deposition in plasma reactors and developing strategies to mitigate this issue are critical steps toward the realization of an industrial plasma-catalytic process for light alkane valorization.

Direct conversion of primary natural gas components (e.g., methane, ethane, propane, and nitrogen) through nonoxidative plasma is especially desirable for small, decentralized processes where oxidative feeds such as steam or CO_2 to mitigate coking may not be consistently available.[11] Numerous works have observed significant coking primarily on exposed electrodes in nonoxidative plasmas, yet little is known about the nature or formation mechanism of the carbon deposits formed in these systems, particularly for nonmethane feeds.[11,13−15] Robertson et al. reported that amorphous hydrocarbon (a-C:H) films formed by plasma enhanced chemical vapor deposition (PECVD) are a class of diamond-like carbons (DLCs) formed by a widely accepted ion bombardment mechanism.[16] Here, the diamond-like character of the carbon refers to its high degree of sp^3-hybridized C−C bonding and low hydrogen content, which give it properties comparable to diamond despite its amorphous structure.[16] However, the low operating pressures and parallel-plate electrode geometry for PECVD are dissimilar to those of high-conversion plasma-catalytic systems, thus requiring additional studies on the coking behavior of atmospheric plasma reactors before comparisons can be made between the two processes. The dynamics of microdischarges and the formation of heterogeneous patterns within the plasma region are also important as they direct the spatial distribution of electron density and may lead to regions of enhanced or diminished carbon deposition rates. Purwins et al. and Guikema et al. independently demonstrated dissipative solitons (DSs), which are stable and localized structures of pseudostationary current density that emerge at regular spatial intervals, resulting in complex and tunable patterns of filaments within the plasma.[17−19] However, a practical understanding of how these plasma macrostructures influence reactor performance through a connection to carbon deposition remains unanswered.

Received: May 17, 2023
Revised: July 13, 2023
Published: July 28, 2023

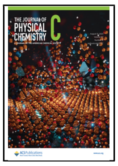

https://doi.org/10.1021/acs.jpcc.3c03268
J. Phys. Chem. C 2023, 127, 15239−15245

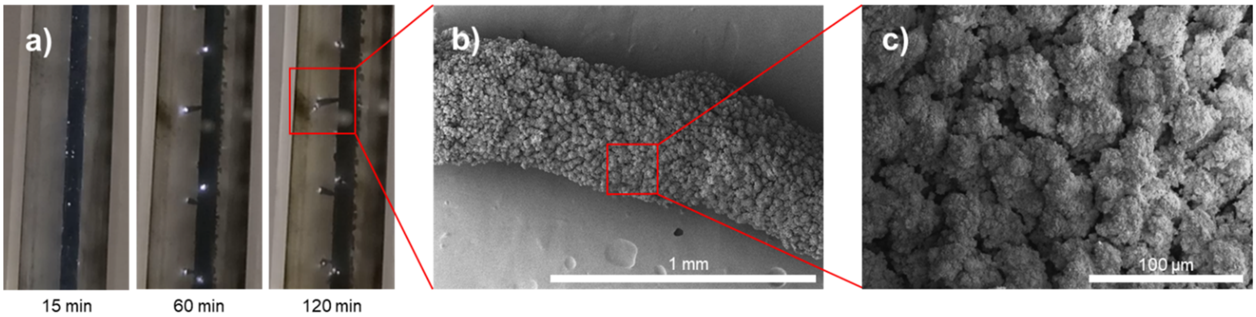

Figure 1. Optical (a) and SEM (b,c) images of *a*-C:H microstructures grown in a 10 W plasma using a 5% ethane in helium feed at 100 mL/min for 120 min.

Here, we report the previously unobserved formation of filamentary DLC structures with long-range order that form in parallel with a traditional DLC film on the inner electrode. These self-organized DLC microstructures are grown using a water-cooled DBD reactor, which provides visual access to the plasma region and allows time-resolved observation of growth within the reactor. The characteristic properties of the DLC microstructures are verified through X-ray Auger Electron Spectroscopy (XAES) and carbon−hydrogen−nitrogen (CHN) elemental analysis, which allows mechanistic comparisons to be made with PECVD-synthesized DLC. Additionally, the incorporation of nitrogen heteroatoms into the a-C:H network to form a-C:H:N as a valuable secondary feedstock is explored as a solution to offset the primary issue of undesirable carbon formation.

2. MATERIALS AND METHODS

2.1. Experimental Setup. The carbon formations were grown using a water-cooled DBD reactor with a 5% ethane (Airgas 99.9% purity), 0%, 20%, 30%, or 95% nitrogen (Airgas 99.999% purity), and balance helium (Airgas 99.997% purity) feed at a total flow rate of 100 mL/min and atmospheric pressure. The water-cooled DBD reactor used here is a quartz tube (5 mm ID; 7 mm OD) with a cooling jacket/ground electrode that extends 7.8 cm along the length of the tube, for a total discharge volume of 0.9 cm^3 (Figure S1). A silica frit is located at the effluent side of the cooling jacket to catch any detached carbon microstructures and easily separate them from the liquid products. The coolant is unaltered, ionized tap water that also serves as the ground electrode and has been chilled to 278 K. The high voltage electrode is a tungsten rod (1.6 mm diameter) inserted through the center of the tube and placed above the silica frit, resulting in a discharge gap of 1.7 mm. Voltage is applied using an Information Unlimited PVM500-2500T plasma generator, and the charge on the DBD is measured using a 1.0 nF monitor capacitor placed in series with the reactor. The waveform of the applied voltage and charge on the DBD is measured by an oscilloscope (Tektronix TBS1052C) with a 1000x voltage attenuator (Tektronix P6015A), and the power dissipated by the plasma is calculated by integration of the charge-voltage plot as described previously.[20]

Before each batch of DLC is synthesized, the reactor is first calcined in air at 823 K for at least 2 h to remove residual carbon deposits. Next, the reactor is purged using helium for 10 min before switching to the desired feed. The plasma power is then adjusted to the desired value within ±0.4 W during the first 5 min of time on stream and maintained throughout. For the samples generated using a 10 and 15 W plasma, microstructures are grown for 2 h. For samples generated at 5 W and with a N_2 feed, the samples are grown for 4 and 6 h respectively to account for the slower growth rate. Post formation, the vertical spacing of the microstructures is measured by using a cathetometer. Next, the liquid products are collected by dissolving in chloroform (ethanol stabilized; ACS grade), filtering through the silica frit of the reactor, and drying under vacuum overnight. The solid hydrocarbon products are collected by washing with acetone (ACS grade) and drying under vacuum overnight. To avoid potential reactions with acetone, the nitrogen-containing solid products are washed only with chloroform and dried under vacuum overnight.

2.2. Characterization. During the carbon growth stage, the plasma phase was characterized by an optical emission spectroscopy (OES) probe (Ocean Optics USB2000+ XR1 spectrometer with THORLABS F280SMA-A collimator and Ocean Insight QP300-1-SR fiber optic cable). Each solid sample was characterized by scanning electron microscopy (SEM), attenuated total reflectance-Fourier transform infrared spectroscopy (ATR-FTIR), Raman spectroscopy, CHN elemental analysis, and XAES. The SEM used here is a Magellan 400. FTIR measurements were performed on a Bruker Vertex 70 FTIR instrument with an ATR cell (Pike Technologies GladiATR) heated to 318 K. A postmeasurement atmospheric correction was applied to each FTIR spectrum to remove atmospheric water and CO_2 signals. Raman spectroscopy was performed by using a Jasco NRS-5100 confocal Raman microscope with a 532 nm excitation laser. The carbon, hydrogen, and nitrogen atomic fractions were determined by CHN analysis using a Costech ECS 4010 EA system. Finally, XAES was conducted on a PHI VersaProbe II.

3. RESULTS AND DISCUSSION

We begin by describing the carbon microstructures shown in Figure 1 and Video S1, which were observed in an annular DBD reactor consisting of an internal tungsten driving electrode and an outer water grounded electrode with the quartz body as the dielectric barrier. The water electrode doubles as a cooling jacket (Figure S1), which chills the reactor to 278 K to minimize thermal reactions, such as thermal cracking of longer chain hydrocarbons that could contribute to carbon deposition. Other details about the experimental procedures can be found in Section 2. The 1−2 mm long microstructures are observed when an ethane feed is diluted to 5% in pure helium, and substitution of the helium diluent with

N_2 was found to fully inhibit microstructure growth, instead resulting in the formation of a thin film on the inner electrode. Time-resolved microstructure growth is shown in Figure 1a, which highlights the prenucleation (0−15 min) and growth (15−120 min) stages. During the prenucleation stage, several corona-like discharges are ignited on the inner electrode for approximately 1−2 s each before they are extinguished. These appear as pinpoints of light on the tungsten electrode and are caused by local electric field enhancement due to surface roughness from the growing *a*-C:H film.[21,22] After 15 min, the ephemeral discharges self-order in regular intervals, forming permanent regions of plasma that rapidly grow individual microstructures. These basic stages are observed for all conditions investigated that form microstructures, and the gas-phase carbon balance for each experiment was between 85% and 95%.

The elemental composition and atomic structure of the microstructures were obtained using CHN elemental analysis and the XAES D-parameter.[23−27] Table 1 shows the hydrogen content and sp^3 carbon fraction of the samples grown with 0% N_2 in the feed at 5, 10, and 15 W (0N-5W, 0N-10W, and 0N-15W). The low hydrogen content and high sp^3 fraction of each sample verify a DLC classification based on definitions provided by Robertson et al.[16] Thus, the mechanism of formation is likely similar to the commonly accepted ion bombardment−subplantation mechanism originally proposed by Lifshitz et al.[16,28] Briefly, this mechanism involves the creation of dangling bonds on the growth surface from hydrogen abstraction and surface etching by CH_X and H radicals.[16] This step is temperature dependent, with surface etching rates increasing with increasing temperature. Growth is propagated by temperature independent CH_X radical addition to the dangling bonds, which produces an amorphous sp^3-carbon film with a high hydrogen content near the surface.[16] The balance between surface etching and CH_X radical addition dictates the overall growth rate, which increases at lower temperatures when chemical erosion by atomic hydrogen is minimized.[16] Low H% DLC is formed by the implantation of high-energy ions, which perform subsurface hydrogen abstraction to remove hydrogen content from underlying layers and create cross-linked sp^3 C−C bonds with desirable mechanical properties.[16] To increase the energy of the incident ions and improve their penetration depth, DLC is typically synthesized in PECVD at low pressures with the substrate on the smaller surface area electrode.[16] This takes advantage of the negative DC self-bias that occurs between the larger and smaller electrodes from residual positive charges in the plasma.[16] Considering the small discharge area of each microstructure growth site compared to that of the ground electrode, this process is likely contributing to the low hydrogen content recorded in Table 1 and could help explain why DLC microstructures are forming at atmospheric pressure. For a more detailed discussion on the mechanism of *a*-C:H film growth, the reader is directed to the excellent review by Jacob.[29]

Table 1. Chemical Structure Properties of Both *a*-C:H and *a*-C:H:N Microstructures Grown with Different N_2 Concentrations and Plasma Powers

Sample	H (mol %)	sp^3 carbon (%)	N/C (by mole)	I_D/I_G
0N-5W	41	81	0.00	0.00
0N-10W	56	71	0.00	0.78
0N-15W	53	61	0.00	0.43
20N-15W	–	–	0.06	0.00
30N-15W	–	–	0.16	0.27
95N-15W	–	–	0.26	0.28

While traditional solutions address the issue of excess carbon deposition through mitigation, an orthogonal solution is used to compensate for the reduced process lifetime through carbon valorization. As an abundant natural resource and a major component of natural gas, nitrogen is a clear candidate for enriching carbon.[21,30−33] However, the incorporation of nitrogen heteroatoms into a carbon framework using thermal routes is both an economically and environmentally expensive process that requires temperatures in excess of 800 °C and a preprocessed nitrogen source (e.g., ammonia from Haber-Bosch, pyridine, or melamine).[34,35] Thus, the direct conversion of N_2 and natural gas to C−N bonds under mild conditions using renewable energy is a significant advancement toward decarbonization while simultaneously reconciling the ubiquitous issue of undesirable carbon deposition in plasma reactors. PECVD studies that produce *a*-C:H:N under nonthermal plasma conditions have shown that changing the N_2/C ratio in the feed allows the properties of the resulting film to be controlled.[21,30,36] In this work, the addition of N_2 to the feed at 20%, 30%, and 95% (20N-15W, 30N-15W, and 95N-15W) successfully resulted in nitrogen-containing solids as well as a significant yield of liquid oligomers that condensed on the walls of the reactor. The solid products were analyzed by CHN (Table 1), and were found to have nitrogen/carbon ratios between 0.06 (1:17) and 0.26 (1:4). To the best of our knowledge, this is the lowest temperature (278 K) ever reported for one-pot carbon−nitrogen coupling directly from N_2. The oligomeric products collected were found to have a higher nitrogen content than the solid products, with nitrogen/carbon ratios (Table S1) ranging from 0.12 (1:5) to 0.33 (1:3). The nitrogen content in all samples increased with increasing nitrogen in the feed, which is consistent with the results obtained by Silva et al. for deposition of *a*-C:H:N films with N_2/CH_4 plasma.[30]

SEM images of the pure hydrocarbon microstructures (Figures 1b−c and S2) show a rough, "cauliflower-like" surface, which is typically seen in other types of plasma-grown carbon structures.[37−40] In contrast, the SEM images of the *a*-C:H:N microstructures (Figure S3) show much smoother features, which suggests that they are composed of viscous polymers rather than a glassy amorphous carbon. The EDX spectrum of 0N-15W shows a small oxygen peak, which is an artifact of the adhesive substrate and is not representative of the sample (Figure S4a−b). However, the EDX analysis of 20N-15W (Figure S4c) shows a much larger oxygen peak, indicating that a non-negligible oxygen content is likely present in the sample. This is confirmed by ATR-FTIR (Figure 2a), and originates from either amine capture of CO_2 or oxidation of residual chloroform solvent to form halogenated carbonyls during storage.[41] The residual chloroform is seen as a chlorine peak in the EDX spectrum and as a C−Cl stretch (748 cm^{-1}) in the ATR-FTIR spectrum (Figure S5),[42] and is likely retained in only the *a*-C:H:N samples due to solvation in the polymeric phase. This also implies the determined N/C mole ratios in Tables 1 and S1 are likely lower than the true values due to excess carbon originating from residual chloroform. Finally, the EDX spectrum of the 20N-15W sample shows a nitrogen peak that is absent for the 0N-15W sample.

https://doi.org/10.1021/acs.jpcc.3c03268
J. Phys. Chem. C 2023, 127, 15239−15245

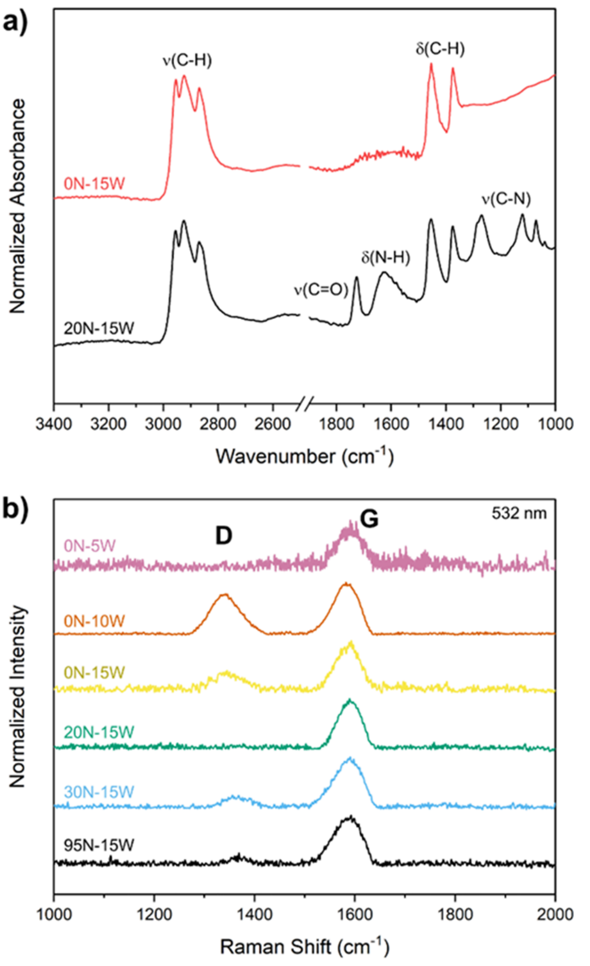

Figure 2. ATR-FTIR (a) and Raman (b) spectroscopies comparing *a*-C:H (0N-5W, 0N-10W, 0N-15W) and *a*-C:H:N (20N-15W, 30N-15W, 95N-15W) samples.

ATR-FTIR spectroscopy was performed on the microstructures to identify major functional groups and verify nitrogen incorporation in the *a*-C:H:N samples (Figure 2). The ATR-FTIR spectra of the *a*-C:H microstructures (Figures 2a and S5) revealed methyl C−H stretching (2954 cm^{-1}), methylene C−H stretching (2924 cm^{-1}; 2869 cm^{-1}), methylene scissoring (1454 cm^{-1}), and methyl rocking (1375 cm^{-1}), which are typical for large, saturated hydrocarbons such as DLC.[43] All *a*-C:H samples showed the same features, and the lack of additional vibrational peaks from heteroatoms such as O, N, or Cl supports the EDX results that the *a*-C:H microstructures contain exclusively carbon and hydrogen. Additionally, no unsaturated features such as aromatic C−H stretching, allyl stretching, or alkyne stretching are observed, indicating that the sp^2 phase is contained in regions of graphite clusters (IR inactive) capped by sp^3 carbons rather than hydrogens.

The ATR-FTIR spectra of each *a*-C:H:N sample show similar features, and a representative spectrum is shown in Figure 2a. The spectra contain all the same saturated hydrocarbon features as those of *a*-C:H, in addition to N−H scissoring (1622 cm^{-1}) from 1° amines,[44] carbonyl stretching (1726 cm^{-1}) from interactions with ambient air,[45] and several features in the fingerprint region (<1400 cm^{-1}) that are assigned to C−N stretching.[44] The amine and C−N features confirm that the nitrogen atoms quantified by CHN are indeed incorporated into the chemical structure of the amorphous hydrocarbons rather than as a N_2 clathrate. The lack of clear N−H stretching features above 3000 cm^{-1} is due to peak broadening from hydrogen bonding with other amines.[44] Additionally, the shoulder at 2245 cm^{-1} in Figure S5 can be assigned to nitrile functional groups.[46] Although nitrile stretching is difficult to observe in this ATR-FTIR system due to poor transmission of the ATR crystal between 2300 and 1900 cm^{-1}, nitrile groups are expected to be present considering they have been observed in large quantities from similar systems of hydrocarbon−nitrogen plasmas.[30]

Raman spectroscopy is a highly informative tool that has been used extensively for studying the sp^2 carbon phase in DLC.[47] We used a 532 nm excitation laser to look at the D and G bands in the microstructures (Figure 2b). The G band (1560 cm^{-1}) arises from stretching vibrations of sp^2 carbon pairs in both rings and chains, and both its position and shape are consistent for all samples analyzed.[47] The D band is a result of ring breathing modes of sp^2 atoms, and its intensity is dependent on both the concentration of sp^2 atoms and the degree of disorder in the ring.[47]

In amorphous carbons, the intensity ratio of the D to G band (I_D/I_G) is taken as a measure of the size of the sp^2 ring-phase, with I_D/I_G decreasing as the size of the graphitic clusters decreases.[47] Each sample has I_D/I_G values below 1.0 (Table 1), which combined with the lack of evidence for alkene stretching in ATR-FTIR (Figure 2a) suggests that the sp^2 phase is predominantly organized into small clusters of ordered aromatic rings. Additionally, the D peak for each *a*-C:H:N sample is blue-shifted by about 25 cm^{-1} compared to the *a*-C:H samples. Although little is known about the effect of nitrogen on the D-band, several works have reported a similar blue-shift in the position of the D-band upon incorporation of nitrogen into both graphene[31,32] and DLC.[36] This shift represents a change in the structure of the graphitic regions of the *a*-C:H:N, suggesting that nitrogen atoms incorporated into the aromatic rings alter the vibrational frequency of the ring breathing in the graphitic phase. Thus, both ATR-FTIR

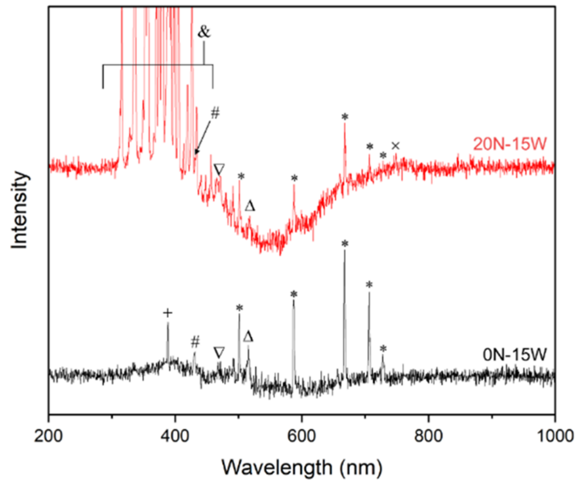

Figure 3. OES of plasma at 20 kHz. 20% N_2 feed at 15 W (red) and 0% N_2 feed at 15 W (black) are shown. Remainder of feed is 5% C_2H_6 and balance He at 100 mL/min total flow. Emission line assignments: (&) N_2 second positive system and N_2^+ first negative system; (+) CH B-X; (#) CH A-X; (Δ) C_2 1−0; (∇) C_2 0−0; (×) N I; (*) He I.

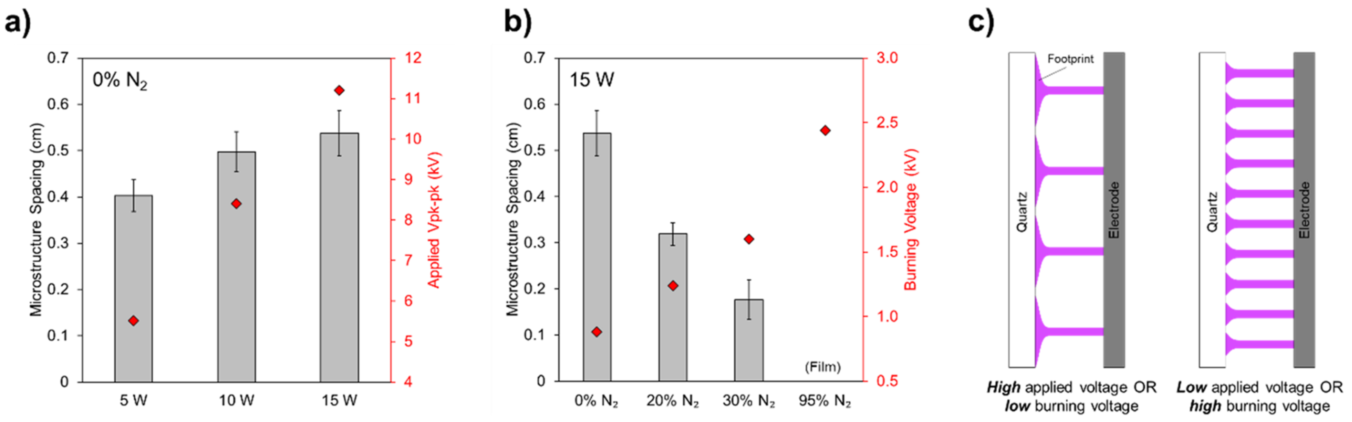

Figure 4. Microstructure spacing dependence on applied voltage (a) and feed composition (b) with microdischarge distributions (c). Feed composition is 5% C_2H_6, 0% N_2, and balance He at 100 mL/min total flow, 278 K, and 15 W discharge power unless otherwise noted.

and Raman spectroscopy together provide evidence that nitrogen is dispersed throughout the sp^2 and sp^3 phases.

Optical emission spectra were recorded at the onset of microstructure nucleation to characterize the plasma phase near the growth site and identify the species present (Figure 3). Although CH_3 and CH_2 radicals are not observable by OES, emission lines associated with both the CH ($B^2\Sigma \rightarrow X^2\Pi$ and $A^2\Delta \rightarrow X^2\Pi$ transitions at 387 and 431.5 nm respectively) and C_2 Swan ($d^3\Pi_g \rightarrow a^3\Pi_u$ transitions with $\Delta\nu = 1$ and $\Delta\nu = 0$ at 473.7 and 516.5 nm respectively) systems are observed in both feeds, confirming the presence of carbon and hydrocarbon radicals near the growth surface for addition to dangling bonds.[48] For nitrogen-containing feeds, additional lines assigned to the N_2 second positive system, the N_2+ first negative system, and atomic nitrogen (N I; 746.8 nm) are observed. The N I line proves that the plasma is dissociating N_2 near the surface, producing reactive atomic nitrogen that combines with either other gas-phase species or the *a*-C:H:N surface to form carbon−nitrogen bonds. This process of N or NH_X radical addition to the surface is likely equivalent to CH_X radical addition proposed in the mechanism by Lifshitz et al.[28]

Lastly, we sought to understand the processes governing how these microstructures form and why they grow in self-ordered patterns. The singular directionality of the microstructure growth from the inner (tungsten) electrode to the outer (quartz) dielectric suggests some dependence on the electrode/dielectric properties. To demonstrate this, the inner electrode was coated with either copper or polyimide tape and compared to bare tungsten to evaluate how the inner electrode material affects microstructure nucleation. Figure S7a−b show similar microstructure growth on both copper and tungsten electrodes, suggesting the metallurgy of the electrode does not play a major role. However, the polyimide barrier in Figure S7c prevented microstructure nucleation, instead promoting the formation of a hydrocarbon film. This clear difference between metal and polyimide surfaces suggests the microstructures nucleate through the adsorption of plasma species on metal sites and thus require a metal substrate to adhere and grow.

The microstructure spacing dependence on feed composition and applied voltage is listed in Figure 4a−b. Each experiment was performed at 100 mL/min total feed, with 5% ethane and the balance of a variable mixture of helium and N_2. As the power and applied voltage are increased, the spacing shows a small increase from 0.40 to 0.54 cm (Figure 4a). Additionally, when the ratio of N_2 to helium in the feed is increased, the spacing dramatically falls from 0.54 cm (0% N_2) to zero, with the eventual formation of a homogeneous film at 95% N_2 in the feed (Figure 4b). These results are consistent with a Type A microdischarge pattern in a one-dimensional DBD observed by Guikema et al.[18] The authors of this study concluded that the spacing of the microdischarges along a linear DBD was determined by the area of the microdischarge footprint, which is a surface discharge known to form at the dielectric barrier (Figure 4c).[18] Moreover, the spacing dependence on N_2 in the feed (Figure 4b) is consistent with a report from Callegari et al., which showed a decrease in stationary microdischarge spacing with increasing gas breakdown voltage (or burning voltage, U_b, if alternating current) from neon to nitrogen.[19] These trends provide evidence that the spacing of the microstructures is determined by the stationary DS pattern before the microstructures begin to nucleate. Indeed, the microdischarge footprints can be seen in Video S1 as localized areas of carbon deposition that appear on the quartz wall during the prenucleation stage, suggesting that the locations of the microdischarges during prenucleation and microstructure formation are linked.

4. CONCLUSIONS

In this study, self-ordered *a*-C:H and *a*-C:H:N microstructures were synthesized with an atmospheric pressure DBD at 278 K. The nitrogen content of the microstructures was found to increase up to 0.26 N/C with increasing N_2 in the feed, and both aliphatic and aromatic C−N bonds were formed in *a*-C:H:N without the use of high temperatures, harmful solvents, or expensive catalysts. Additionally, the microstructures were found to only grow on metal substrates, and the spacing of their formation was in good agreement with a Type A microdischarge pattern determined by DS self-ordering behavior.[18] Although the range of conditions that facilitate microstructure growth appears to be narrow, it is likely that other combinations of feed composition, plasma properties, and reactor configuration will result in similar structures. Thus, this knowledge of time-resolved and spatially defined carbon growth will help inform microkinetic modeling and reactor design for other hydrocarbon plasma technologies, particularly for longer time-on-stream applications, where carbon deposits are significant. Although additional questions remain about the impact of film growth versus microstructure growth on the process lifetime, the connection between electron density patterns and coke formation allows for greater control over carbon deposition in nonoxidative hydrocarbon plasma reactors.

■ ASSOCIATED CONTENT

Supporting Information

The Supporting Information is available free of charge at https://pubs.acs.org/doi/10.1021/acs.jpcc.3c03268.

> Experimental methods, table of additional sample properties, additional SEM images, EDX profiles, full ATR-FTIR spectra, charge-voltage plots, and photographs of different electrode materials (PDF)
>
> Video S1: Time-lapse video of 0N-10W growth (MP4)

■ AUTHOR INFORMATION

Corresponding Author

Jason C. Hicks − *Department of Chemical and Biomolecular Engineering, University of Notre Dame, Notre Dame, Indiana 46556, United States;* orcid.org/0000-0002-5054-2874; Email: Jhicks3@nd.edu

Author

Russell J. Clarke − *Department of Chemical and Biomolecular Engineering, University of Notre Dame, Notre Dame, Indiana 46556, United States*

Complete contact information is available at: https://pubs.acs.org/10.1021/acs.jpcc.3c03268

Notes

The authors declare no competing financial interest.

■ ACKNOWLEDGMENTS

This work is partially supported by the Engineering Research Centers Program of the National Science Foundation under NSF Cooperative Agreement No. EEC1647722 and by the U.S. Department of Energy, Office of Fossil Energy, Office of Natural Gas and Petroleum Technology, through the National Energy Technology Laboratory, under Award No. DE-FE0031862. The authors thank the Notre Dame Materials Characterization Facility, the Notre Dame Center for Environmental Science and Technology, the Notre Dame Integrated Imaging Facility, and the Notre Dame Schleckser Family Unit Operations Laboratory for use of their equipment and facilities.

■ REFERENCES

(1) Kim, J.; Abbott, M. S.; Go, D. B.; Hicks, J. C. Enhancing C-H Bond Activation of Methane via Temperature-Controlled, Catalyst-Plasma Interactions. *ACS Energy Lett.* **2016**, *1* (1), 94−99.

(2) Labinger, J. A.; Bercaw, J. E. Understanding and Exploiting C−H Bond Activation. *Nature* **2002**, *417* (6888), 507−514.

(3) Gradassi, M. J.; Wayne Green, N. Economics of Natural Gas Conversion Processes. *Fuel Process. Technol.* **1995**, *42* (2−3), 65−83.

(4) Zhang, L.; Heijkers, S.; Wang, W.; Martini, L. M.; Tosi, P.; Yang, D.; Fang, Z.; Bogaerts, A. Dry Reforming of Methane in a Nanosecond Repetitively Pulsed Discharge: Chemical Kinetics Modeling. *Plasma Sources Sci. Technol.* **2022**, *31*, No. 055014.

(5) Tu, X.; Gallon, H. J.; Twigg, M. V.; Gorry, P. A.; Whitehead, J. C. Dry Reforming of Methane over a Ni/Al2O3 Catalyst in a Coaxial Dielectric Barrier Discharge Reactor. *J. Phys. D Appl. Phys.* **2011**, *44* (27), No. 274007.

(6) Alcala, R.; Dean, D. P.; Chavan, I.; Chang, C.-W.; Burnside, B.; Pham, H. N.; Peterson, E.; Miller, J. T.; Datye, A. K. Strategies for Regeneration of Pt-Alloy Catalysts Supported on Silica for Propane Dehydrogenation. *Appl. Catal. A Gen* **2023**, *658*, No. 119157.

(7) Bogaerts, A.; Tu, X.; Whitehead, J. C.; Centi, G.; Lefferts, L.; Guaitella, O.; Azzolina-Jury, F.; Kim, H. H.; Murphy, A. B.; Schneider, W. F.; et al. The 2020 Plasma Catalysis Roadmap. *J. Phys. D: Appl. Phys.* **2020**, *53*, No. 443001.

(8) Mehta, P.; Barboun, P.; Herrera, F. A.; Kim, J.; Rumbach, P.; Go, D. B.; Hicks, J. C.; Schneider, W. F. Overcoming Ammonia Synthesis Scaling Relations with Plasma-Enabled Catalysis. *Nat. Catal* **2018**, *1* (4), 269−275.

(9) Clarke, R. J.; Hicks, J. C. Interrogation of the Plasma-Catalyst Interface via In Situ/Operando Transmission Infrared Spectroscopy. *ACS Engineering Au* **2022**, *2*, 535−546.

(10) AlQahtani, M. S.; Wang, X.; Knecht, S. D.; Bilén, S. G.; Song, C. Plasma-Enhanced Catalytic Reduction of SO2: Decoupling Plasma-Induced Surface Reaction from Plasma-Phase Reaction. *Appl. Catal., B* **2021**, *286*, No. 119852.

(11) Scapinello, M.; Delikonstantis, E.; Stefanidis, G. D. The Panorama of Plasma-Assisted Non-Oxidative Methane Reforming. *Chemical Engineering and Processing: Process Intensification* **2017**, *117*, 120−140.

(12) Belov, I.; Paulussen, S.; Bogaerts, A. Appearance of a Conductive Carbonaceous Coating in a CO $_2$ Dielectric Barrier Discharge and Its Influence on the Electrical Properties and the Conversion Efficiency. *Plasma Sources Sci. Technol.* **2016**, *25* (1), No. 015023.

(13) Wang, D. W.; Ma, T. C.; Zhang, Y. T. Study on Natural Gas Converted to C_2 Hydrocarbons in Plasma State. *Adv. Mat Res.* **2011**, *383−390*, 2894−2899.

(14) Khalifeh, O.; Taghvaei, H.; Mosallanejad, A.; Rahimpour, M. R.; Shariati, A. Extra Pure Hydrogen Production through Methane Decomposition Using Nanosecond Pulsed Plasma and Pt−Re Catalyst. *Chemical Engineering Journal* **2016**, *294*, 132−145.

(15) Kim, J.; Go, D. B.; Hicks, J. C. Synergistic Effects of Plasma−Catalyst Interactions for CH $_4$ Activation. *Phys. Chem. Chem. Phys.* **2017**, *19* (20), 13010−13021.

(16) Robertson, J. Diamond-like Amorphous Carbon. *Materials Science and Engineering: R: Reports* **2002**, *37* (4−6), 129−281.

(17) Purwins, H.-G.; Bödeker, H. U.; Amiranashvili, Sh. Dissipative Solitons. *Adv. Phys.* **2010**, *59* (5), 485−701.

(18) Guikema, J.; Miller, N.; Niehof, J.; Klein, M.; Walhout, M. Spontaneous Pattern Formation in an Effectively One-Dimensional Dielectric-Barrier Discharge System. *Phys. Rev. Lett.* **2000**, *85* (18), 3817−3820.

(19) Callegari, T.; Bernecker, B.; Boeuf, J. P. Pattern Formation and Dynamics of Plasma Filaments in Dielectric Barrier Discharges. *Plasma Sources Sci. Technol.* **2014**, *23* (5), No. 054003.

(20) Peeters, F.; Butterworth, T. Electrical Diagnostics of Dielectric Barrier Discharges. In *Atmospheric Pressure Plasma - from Diagnostics to Applications*; IntechOpen: 2019. DOI: 10.5772/intechopen.80433.

(21) Amaratunga, G. A. J.; Silva, S. R. P. Nitrogen Containing Hydrogenated Amorphous Carbon for Thin-film Field Emission Cathodes. *Appl. Phys. Lett.* **1996**, *68* (18), 2529−2531.

(22) Grill, A. Electrical and Optical Properties of Diamond-like Carbon. *Thin Solid Films* **1999**, *355−356*, 189−193.

(23) Lascovich, J. C.; Rosato, V. Analysis of the Electronic Structure of Hydrogenated Amorphous Carbon via Auger Spectroscopy. *Appl. Surf. Sci.* **1999**, *152* (1−2), 10−18.

(24) Lascovich, J. C.; Santoni, A. Study of the Occupied Electronic Density of States of Carbon Samples by Using Second Derivative Carbon KVV Auger Spectra. *Appl. Surf. Sci.* **1996**, *103* (3), 245−253.

(25) Lascovich, J. C.; Giorgi, R.; Scaglione, S. Evaluation of the Sp2/Sp3 Ratio in Amorphous Carbon Structure by XPS and XAES. *Appl. Surf. Sci.* **1991**, *47* (1), 17−21.

(26) Lascovich, J. C.; Scaglione, S. Comparison among XAES, PELS and XPS Techniques for Evaluation of Sp2 Percentage in a-C:H. *Appl. Surf. Sci.* **1994**, *78* (1), 17−23.

(27) Morgan, D. J. Comments on the XPS Analysis of Carbon Materials. *C (Basel)* **2021**, 7 (3), 51.

(28) Lifshitz, Y.; Kasi, S. R.; Rabalais, J. W.; Eckstein, W. Subplantation Model for Film Growth from Hyperthermal Species. *Phys. Rev. B* **1990**, *41* (15), 10468−10480.

(29) Jacob, W. Surface Reactions during Growth and Erosion of Hydrocarbon Films. *Thin Solid Films* **1998**, *326* (1−2), 1−42.

(30) Silva, S. R. P.; Robertson, J.; Amaratunga, G. A. J.; Rafferty, B.; Brown, L. M.; Schwan, J.; Franceschini, D. F.; Mariotto, G. Nitrogen Modification of Hydrogenated Amorphous Carbon Films. *J. Appl. Phys.* **1997**, *81* (6), 2626−2634.

(31) Podila, R.; Chacón-Torres, J.; Spear, J. T.; Pichler, T.; Ayala, P.; Rao, A. M. Spectroscopic Investigation of Nitrogen Doped Graphene. *Appl. Phys. Lett.* **2012**, *101* (12), No. 123108.

(32) Matsoso, B. J.; Ranganathan, K.; Mutuma, B. K.; Lerotholi, T.; Jones, G.; Coville, N. J. Time-Dependent Evolution of the Nitrogen Configurations in N-Doped Graphene Films. *RSC Adv.* **2016**, *6* (108), 106914−106920.

(33) Martini, A. M.; Walter, L. M.; Ku, T. C. W.; Budai, J. M.; McIntosh, J. C.; Schoell, M. Microbial Production and Modification of Gases in Sedimentary Basins: A Geochemical Case Study from a Devonian Shale Gas Play, Michigan Basin. *Am. Assoc Pet Geol Bull.* **2003**, *87* (8), 1355−1375.

(34) Inagaki, M.; Toyoda, M.; Soneda, Y.; Morishita, T. Nitrogen-Doped Carbon Materials. *Carbon N Y* **2018**, *132*, 104−140.

(35) Wei, D.; Liu, Y.; Wang, Y.; Zhang, H.; Huang, L.; Yu, G. Synthesis of N-Doped Graphene by Chemical Vapor Deposition and Its Electrical Properties. *Nano Lett.* **2009**, *9* (5), 1752−1758.

(36) Shiao, J.; Hoffman, R. W. Studies of Diamond-like and Nitrogen-Containing Diamond-like Carbon Using Laser Raman Spectroscopy. *Thin Solid Films* **1996**, *283* (1−2), 145−150.

(37) Kozak, D.; Shibata, E.; Iizuka, A.; Nakamura, T. Growth of Carbon Dendrites on Cathode above Liquid Ethanol Using Surface Plasma. *Carbon N Y* **2014**, *70*, 87−94.

(38) Sobczyk, A. T.; Jaworek, A. Carbon Microstructures Synthesis in Low Temperature Plasma Generated by Microdischarges. *Applied Sciences* **2021**, *11* (13), 5845.

(39) Chhowalla, M.; Teo, K. B. K.; Ducati, C.; Rupesinghe, N. L.; Amaratunga, G. A. J.; Ferrari, A. C.; Roy, D.; Robertson, J.; Milne, W. I. Growth Process Conditions of Vertically Aligned Carbon Nanotubes Using Plasma Enhanced Chemical Vapor Deposition. *J. Appl. Phys.* **2001**, *90* (10), 5308−5317.

(40) Danilaev, M. P.; Bogoslov, E. A.; Pol'skii, Yu. E.; Nasybullin, A. R.; Pudovkin, M. S.; Khadiev, A. R. Structure of Carbon Dendrites Obtained in an Atmospheric-Pressure Gas Discharge. *Technical Physics* **2017**, *62* (2), 255−260.

(41) Clover, A. M. The Auto-Oxidation of Chloroform. *J. Am. Chem. Soc.* **1923**, *45* (12), 3133−3138.

(42) Lin-Vien, D.; Colthup, N. B.; Fateley, W. G.; Grasselli, J. G. Halocompounds. In *The Handbook of Infrared and Raman Characteristic Frequencies of Organic Molecules*; Elsevier: 1991; pp 29−44. DOI: 10.1016/B978-0-08-057116-4.50009-2.

(43) Lin-Vien, D.; Colthup, N. B.; Fateley, W. G.; Grasselli, J. G. Alkanes. In *The Handbook of Infrared and Raman Characteristic Frequencies of Organic Molecules*; Elsevier: 1991; pp 9−28. DOI: 10.1016/B978-0-08-057116-4.50008-0.

(44) Lin-Vien, D.; Colthup, N. B.; Fateley, W. G.; Grasselli, J. G. Compounds Containing −NH2, −NHR, and −NR2 Groups. In *The Handbook of Infrared and Raman Characteristic Frequencies of Organic Molecules*; Elsevier: 1991; pp 155−178. DOI: 10.1016/B978-0-08-057116-4.50016-X.

(45) Lin-Vien, D.; Colthup, N. B.; Fateley, W. G.; Grasselli, J. G. Compounds Containing the Carbonyl Group. In *The Handbook of Infrared and Raman Characteristic Frequencies of Organic Molecules*; Elsevier: 1991; pp 117−154. DOI: 10.1016/B978-0-08-057116-4.50015-8.

(46) Lin-Vien, D.; Colthup, N. B.; Fateley, W. G.; Grasselli, J. G. The −C═N and −N═C Groups. In *The Handbook of Infrared and Raman Characteristic Frequencies of Organic Molecules*; Elsevier: 1991; pp 105−115. DOI: 10.1016/B978-0-08-057116-4.50014-6.

(47) Ferrari, A. C. Non-Destructive Characterisation of Carbon Films. In *Tribology of Diamond-Like Carbon Films*; Springer US: Boston, MA, pp 25−82. DOI: 10.1007/978-0-387-49891-1_2.

(48) Heintze, M.; Magureanu, M.; Kettlitz, M. Mechanism of C2 Hydrocarbon Formation from Methane in a Pulsed Microwave Plasma. *J. Appl. Phys.* **2002**, *92* (12), 7022−7031.